



Bimetallic (Cu, Zn) ZIF-derived S-scheme heterojunction for efficient remediation of aqueous pollutants in visible light/peroxymonosulfate system

Tianren Li^{a,b,c}, Mingyu Li^{a,b,c}, Jingjing Jiang^{a,b,c}, Ziqing Zhao^{a,b,c}, Zhongxu Li^{a,b,c}, Chunrui Zhao^{a,b,c}, Xinyu Wang^{a,b,c}, Shuangshi Dong^{a,b,c,*}

^a Key Laboratory of Groundwater Resources and Environment (Jilin University), Ministry of Education, Jilin University, Changchun 130021, Jilin, China

^b Chongqing Research Institute, Jilin University, 401120 Chongqing, China

^c Jilin Provincial Key Laboratory of Water Resources and Environment, Jilin University, Changchun 130021, Jilin, China

ARTICLE INFO

Keywords:

Peroxyoxymonosulfate
Photo-assisted Fenton-like reaction
S-scheme heterojunction
Surface metal sites
Reaction mechanism

ABSTRACT

The design of suitable catalyst is the bottleneck in the photo-assisted Fenton-like reaction system. Here we constructed a S-scheme heterojunction consisted of CuO and Cu doped ZnO using Cu-ZIF-8 as precursor. The as-prepared composite catalyst possesses outstanding catalytic activation performance and broad-spectrum degradation capacity. To clearly fit and describe the overall reaction, a pseudo-third-order kinetic model was developed based on the second-order peroxyoxymonosulfate (PMS) consumption and first-order methylene blue removal. The catalyst/visible light/PMS composite reaction system provides remarkable mineralization and anti-interference ability, and is environmental friendliness. The interaction of Cu/Zn bimetallic sites realized the effective utilization of PMS, accelerated the PMS activation and promoted the formation of the highly oxidative $\text{SO}_5^{\bullet-}$. Overall, this work provides new systematic insights on PMS activation by Cu/Zn bimetallic oxide S-scheme heterojunction and is of significance for sewage purification.

1. Introduction

Peroxyoxymonosulfate (PMS) based advanced oxidation process (AOP) has attracted increasing attention in the field of water pollution control due to its strong reactivity and high mineralization potential [1,2]. Among many heterogeneous PMS activation methods, the catalyst/light/PMS mediated composite strategy can realize the synergistic coupling of photocatalysis and Fenton-like reaction, maximizing the utilization of catalyst and PMS [3,4]. However, the efficient removal of the contaminant is still restrained by the sluggish activity of the catalysts.

Zinc oxide (ZnO) has been applied to photo-assisted Fenton-like reaction systems due to its catalytic activation performance [5,6]. However, the wide band gap structure and high carrier recombination rate of the pristine ZnO make it difficult to efficiently utilize the external light energy [7,8]. The ZnO prepared by conventional methods may not be sufficient to provide sufficient adsorption and activation sites, resulting in weak PMS activation efficiency [6]. Undoubtedly, these problems

limit the effective application of ZnO in the light-assisted Fenton-like system.

Recent studies have shown that the S-scheme heterojunction composites can provide the photogenerated carriers with longer lifetime and higher energy for the photo-assisted Fenton-like system, accompanied by lower transition metal leaching of the catalyst [9]. Conventionally, CuO is utilized as a reduction component to construct S-scheme heterojunction, which also contains soluble Cu(I) with effective PMS activation capability [10,11]. Nevertheless, limited CuO/ZnO were reported as S-scheme heterojunction owing to the unmatched Fermi levels [12,13]. The dopant of Cu which is selected for its similar atomic properties with Zn, can tailor the energy band position and Fermi level of ZnO, providing the possibility for the construction of S-scheme heterojunction [14,15]. Moreover, the metal atom doping would further improve the energy usage efficiency of the catalyst [16].

ZnO derived from the Zeolitic Imidazolate Framework-8 (ZIF-8) may partially retain the porous morphology of the precursor, providing more active sites on surface and higher light utilization [17,18]. The

* Corresponding author at: Key Laboratory of Groundwater Resources and Environment (Jilin University), Ministry of Education, Jilin University, Changchun 130021, Jilin, China.

E-mail address: dongshuangshi@gmail.com (S. Dong).

<https://doi.org/10.1016/j.apcatb.2023.122539>

Received 6 January 2023; Received in revised form 22 February 2023; Accepted 25 February 2023

Available online 26 February 2023

0926-3373/© 2023 Elsevier B.V. All rights reserved.

bimetallic X-ZIF-8 (X = Co, Cu, etc.) could be synthesized by replacing the Zn metal node with a single metal can be served as a derivative template to fabricate transition metal doped ZnO [19,20]. Besides, studies have shown that excessive cation doping would cause the lattice collapse and form new metal oxide crystal phases [21]. In view of the above, we assumed that the CuO and Cu-doped ZnO composite might be directly formed by using Cu-ZIF-8 synthesized with Cu-rich conditions as precursor and the as-prepared composite heterojunction was expected to be constructed into a S-scheme heterojunction.

Thus, we proposed to synthesize Cu, Zn bimetallic oxide using Cu-ZIF-8 as deriving precursor to construct the heterojunction of CuO and Cu-doped ZnO. The detailed characterization and evaluation were employed to examine the properties of the as-prepared catalysts. The effects of the introduction of the variable-valent transition metal Cu and the participation mechanism of ZnO were elucidated. The possible catalytic activation mechanism of the reaction system was proposed. This work would provide new systematic insights on activation of PMS by S-scheme heterojunction for water purification.

2. Experimental

All reagents were used directly without further purification. CuZnO was derived from Cu-ZIF-8 prepared by a co-synthesis method, and the specific process was as follows. Stoichiometric amount of $\text{Cu}(\text{NO}_3)_2 \cdot 3\text{H}_2\text{O}$ (0.572, 0.763, 0.953, 1.144 g) and 2.348 g $\text{Zn}(\text{NO}_3)_2 \cdot 6\text{H}_2\text{O}$ were dissolved in 160 mL methanol to obtain solution A, while 5.192 g 2-methylimidazole was dissolved in 160 mL methanol to obtain solution B. Subsequently, solution A was quickly transferred to solution B under vigorous stirring at room temperature for 120 min. The resulted precipitation was collected and washed with anhydrous ethanol for several times before drying at 70 °C overnight to obtain Cu-ZIF-8. The collected Cu-ZIF-8 with fully grinding was annealed at 600 °C for 120 min at a heating rate of 5 °C/min. The derived products were designated as CuZnO-x, where x was 1, 2, 3 and 4 in order of the $\text{Cu}(\text{NO}_3)_2 \cdot 3\text{H}_2\text{O}$ dosage from low to high. The pristine ZnO nanoparticles (NPs) was

fabricated by similar methods without introducing $\text{Cu}(\text{NO}_3)_2 \cdot 3\text{H}_2\text{O}$.

A 150 W xenon lamp (CEL-HXF 300, Beijing Education Au-light Co., Ltd) with a 420 nm cut-off filter was chosen as the light source. The methylene blue (MB), rhodamine B (RhB), tetracycline hydrochloride (TCH), carbamazepine (CBZ) and bisphenol A (BPA) were chosen as the target pollutants, respectively. In a typical catalytic degradation test, 2 mg of catalyst was completely mixed with 50 mL pollutant solution. Prior to irradiation, the suspension was thoroughly stirred for 60 min in the dark to achieve an adsorption-desorption equilibrium, and then 0.05 mmol PMS was added to the suspension. During the irradiation, the suspension was sampling every 2 min and filtrated by a 0.22 μm membrane. The repeatability of the photocatalysts were tested by repeating the experiments for five times. The pollutant removal performance of the as-prepared catalyst in actual water was estimated by using tap water and mixed wastewater effluent from a chemical industrial base (consisting of MB, chlorobenzenes, nitrochlorobenzene and chloroaniline etc.) as water substrates.

The scavenger quenching experiments were carried out by a controlled variable method, and the capture agent was added before stirring in dark. Aniline (1.0 mM), methanol (1.0 mM), TEMPOL (1.0 mM), L-histidine (1.0 mM) and isopropanol (1.0 mM) were applied as the scavengers for $\text{SO}_5^{\bullet-}$, $\text{SO}_4^{\bullet-}$, $\bullet\text{O}_2^-$, $^1\text{O}_2$ and $\bullet\text{OH}$, respectively.

The detailed information of material characterizations, analytical methods and DFT computation were provided in the Text S1 of [supplement information](#).

3. Results and discussion

3.1. Catalysts characterization

Fig. 1a presented the TEM images of ZIF-8 derived ZnO and the CuZnO bimetallic oxide. The pristine ZnO NPs possessed relatively uniform polyhedron morphology with the particle size of about 90 nm, while the apparent structure of Cu-ZIF-8 derivatives CuZnO-3 synthesized under Cu^{2+} -rich condition appeared disorganized, which could

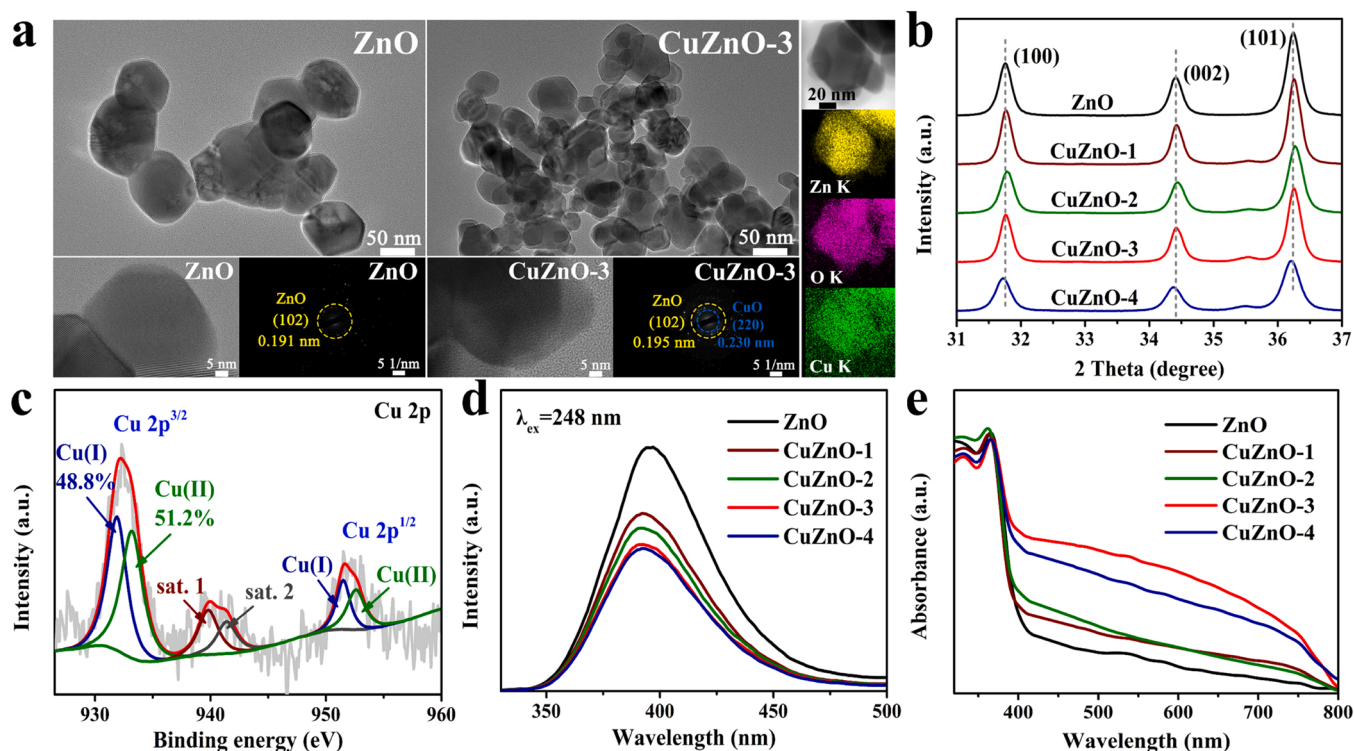


Fig. 1. (a) TEM, HRTEM and SAED of ZnO and CuZnO-3, and STEM image of CuZnO-3 with EDX elemental mapping (Zn, O and Cu); (b) the XRD partial magnification (31°–37°) patterns of as-prepared catalysts; (c) the Cu 2p XPS spectra of CuZnO-3; the (d) PL and (e) UV-vis DRS spectra of all as-prepared catalysts.

also be observed in the SEM images (Fig. S1). The HRTEM and corresponding selected area electron diffraction (SAED) results further demonstrated the influence of Cu introduction on the microstructure. The clear diffraction spot ring shown in the SAED pattern of ZnO was corresponding to the (102) crystal plane of ZnO phase, while the corresponding lattice spacing of CuZnO-3 was slightly increased due to the doping of Cu ions [22]. Furthermore, it could be observed that the CuO phase was appearing in the CuZnO-3. All the elements were evenly distributed in the images of STEM-EDX elemental mapping, demonstrating the homogeneous texture of the semiconductor material.

The XRD patterns of the as-prepared materials further revealed the good crystallization. As shown in Fig. S2, all the patterns showed strong and sharp characteristic peaks, matching the hexagonal wurtzite phase ZnO (ICDD: 36–1451). The weak CuO phase (ICDD: 48–1548) was observed in the CuZnO samples, and the relative peak intensity was positively correlated with the Cu concentration. The slight shift could be observed in the partial magnified XRD pattern of CuZnO samples (Fig. 1b). This was due to the substitution of Cu to Zn sites in the wurtzite phase [23]. It could be inferred that Cu^{2+} initially existed in the form of substituting Zn^{2+} sites in Cu-ZIF-8, and then some lattices with high Cu content collapsed and transformed into CuO phase during the annealing process, while the remaining Cu in the ZnO phase still behaved as dopant ions. Therefore, the CuZnO bimetallic oxide was a heterojunction composed of CuO and Cu-doped ZnO. This co-synthesis preparation method might be beneficial for the transfer and utilization of charges between the interface of each component in the heterojunction [24]. Moreover, the full width at half maximum of CuZnO were also changed compared with the pristine ZnO, indicating the alter of nanoparticle size according to the Debye-Scherrer equation [25]. Combined with the BET-BJH results displayed in Fig. S3 with the detailed description provided in Text S2, it could be summarized that the introduction of Cu would increase the specific surface area of the catalyst in a certain thereby providing more reaction sites [26].

The survey XPS spectra of ZnO and CuZnO-3 in Fig. S4 confirmed the coexisting of each element in the catalysts. Fig. 1c exhibited cleavage peaks of Cu $2p^{3/2}$ and Cu $2p^{1/2}$, which could be further deconvoluted by Gaussian fitting. The lower binding energy part (932.0 and 951.6 eV) was interpreted as Cu(I) while the higher binding energy part (933.3 and 952.7 eV) were corresponding to Cu(II) valence state [27]. The abundant reductive Cu(I) might be generated by the reduction of organic ligands during high temperature annealing [28,29]. In addition, the satellite characteristics at 939.9 and 941.5 eV were specific to the Cu(II) oxidation state [30]. The reduction degree of Cu species could be further judged by the ratio of the intensity of the satellite peak to the main peak, which is expressed as $I_{\text{sat}}/I_{\text{main}}$, where a lower ratio indicated a higher reduction of Cu [31]. The $I_{\text{sat}}/I_{\text{main}}$ values of CuZnO-3 was 27.9%, which was considered to be quite low, indicating that Cu element on the surface of CuZnO-3 possessed a high reduction state. In Fig. S5a, the fragmentation peak spacings of the Zn 2p orbitals were about 23 eV for ZnO and CuZnO-3, confirming the existence of the Zn^{2+} ionic lattice [32]. In comparison with that of ZnO, the Zn $2p^{3/2}$ of CuZnO-3 was shifted to 1021.6 eV, while Zn $2p^{1/2}$ was shifted to 1044.2 eV from 1043.9 eV. This was originated from the asymmetric distribution of electrons caused by the formation of Cu-Zn bimetallic oxide [33]. The O 1s signals of two catalysts (Fig. S5b) could both be deconvoluted into two peaks assigned to lattice oxygen and oxygen vacancy, located at 530.3 and 532.0 eV, respectively [34]. The oxygen vacancies might be formed in the high-temperature calcination process [35].

The room temperature PL spectra in Fig. 1d illustrated that the near band edge emission peaks of CuZnO samples shifted to the low wavelength side as compared with that of pristine ZnO, which was caused by the strong exchange interaction between the 'd' electrons of Cu and the 's' and 'p' electrons of ZnO [16]. Notably, the PL intensity of the CuZnO catalyst was significantly reduced and negatively correlated with the concentration of introduced Cu, indicating that the construction of bimetallic oxide would restrain the exciton recombination. This might

be attributed to the synergy effect of following two aspects, (1) Cu doping provided a competitive pathway for exciton recombination, and (2) the heterojunction formed by CuO modification enhanced the electron-hole separation efficiency [14,36]. The optimum photo-generated carrier separation and conduction capability of CuZnO-3 was also confirmed by transient photocurrent response (Fig. S6a) and electrochemical impedance spectrum (Fig. S6b), which could be attributed to the appropriate heterojunction structure of CuZnO-3 [37].

The results of UV-vis DRS (Fig. 1e) showed that all the as-prepared catalysts exhibited strong light absorption in the ultraviolet region, which accorded with the wide band gap characteristic of ZnO. The CuZnO catalysts possessed enhanced light absorption capacity in the visible light region with the highest absorption of CuZnO-3. This was caused by the modification of CuO with superior visible light response and the existence of impurity level [16,38]. The apparent absorption edges of CuZnO displayed a slight red-shifted compared to the pristine ZnO, and the energy band gap (E_g) of CuZnO-3 was 2.96 eV, lower than that of ZnO at 3.14 eV (Fig. S7). These results demonstrated that the introduction of Cu had positive significance for the improvement of visible light utilization.

3.2. Catalytic performance and kinetics study

The catalytic degradation performance of the as-prepared samples under the vis/PMS system using MB as the target pollutant was shown in Fig. 2a. PMS alone could hardly remove the pollutant in the absence of catalyst. Single photocatalysis (Fig. S8a) or Fenton-like (Fig. S8b) system showed unremarkable degradation efficiency of MB in 10 min reaction, which was lower than 25% and 40%, respectively. In contrast, the photo-assisted Fenton-like system with co-presence of catalyst, PMS and visible light irradiation displayed the superb MB removal efficiency > 80%. This suggested that the degradation under the photo-assisted Fenton-like system was a synergistic coupling of photocatalysis and PMS activation. The CuZnO-3 possessed the highest MB removal efficiency (~100%) and TOC removal efficiency (58.9% from Fig. 2b) under the photo-assisted Fenton-like system in 10 min.

The possible degradation pathways of MB for CuZnO-3/vis/PMS system were proposed from the MB degradation intermediates identified by liquid chromatograph mass spectrometer results (Fig. S9) and displayed in Fig. S10, while the possible intermediate products were listed in Table S1. The MB molecule ($m/z = 284$) first underwent hydroxylation and demethylation [39]. Afterwards, the branched chains on the benzene ring were further removed by dihydroxylation, deamination and demethylation [40]. The formed aromatic compounds with simpler structures were gradually cracked into smaller organic fragments through the above-mentioned functions and ring-opening reactions. Finally, a variety of small molecular weight organic compounds and inorganic substances (such as CO_2 , H_2O and NH_4^+) were generated. In addition, the biotoxicity of the degradation intermediates and catalysts was evaluated (Fig. S11, Text S3). The comprehensive analysis of the results verified that CuZnO-3 and its mediated catalytic degradation of MB could be identified as environmentally friendly.

To further determine the activation of PMS during the catalytic reaction, the consumption rate of PMS was monitored (Fig. 2c) [41]. Combined with the established relationship curves between MB removal and PMS consumption (Fig. S12), it could be concluded that the MB removal rate was positively correlated with the PMS consumption rate, which showed the importance of the PMS activation process for the pollutant degradation reaction. The reaction kinetics study (corresponding evaluation method provided in Text S4) showed that poor fittings were obtained by pseudo-first-order and pseudo-second-order kinetics for the photo-assisted Fenton-like reactions in Fig. S13 and Table S2. As reported, the PMS consumption rate may follow a second-order reaction, and the generated reactive species are directly proportional to $[\text{PMS}]^2$ [42]. Hence, the pseudo-third-order kinetic fitting were carried out based on the second-order PMS consumption

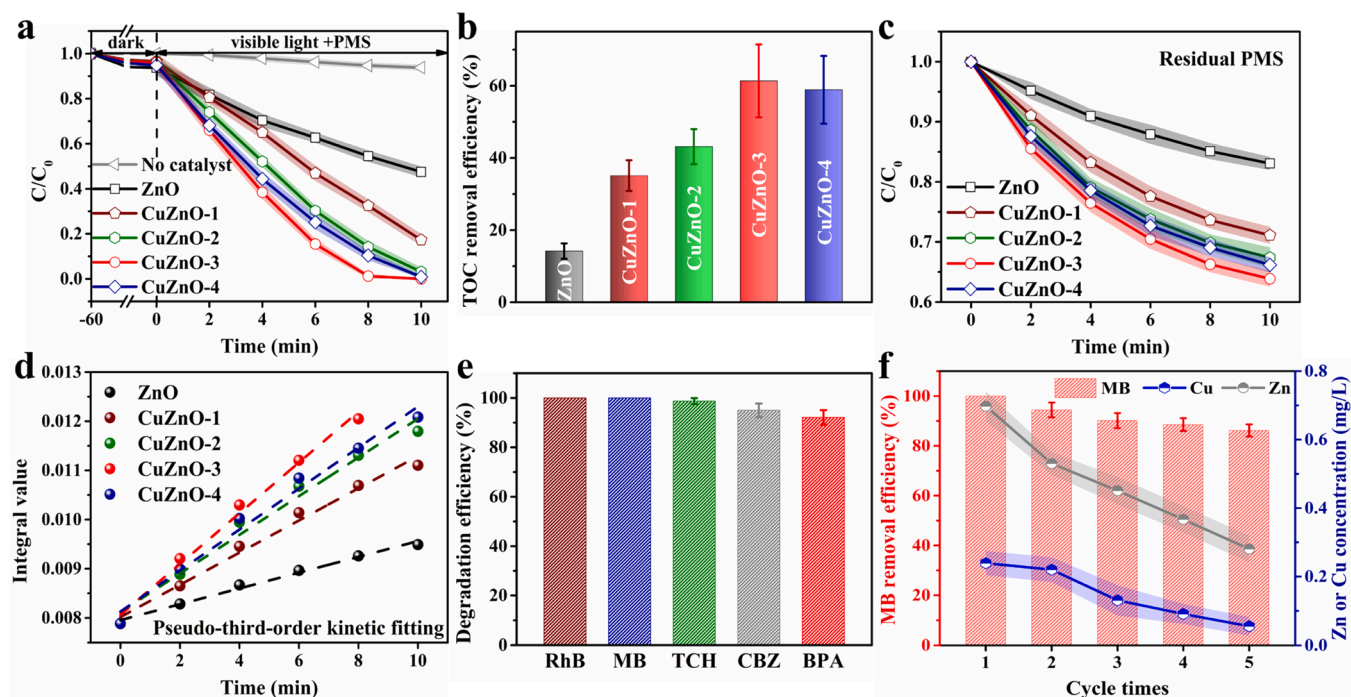


Fig. 2. (a) MB degradation efficiencies, (b) TOC removal efficiencies of MB, (c) PMS consumption rate and (d) corresponding apparent rate constant curves obtained by pseudo-third-order kinetic fitting of all as-prepared catalysts in the photo-assisted Fenton-like system; (e) removal of various representative contaminants by CuZnO-3/vis/PMS reaction system in 10 min; (f) recycling tests and corresponding leached Zn and Cu ions concentration of CuZnO-3. Experimental conditions: $[MB]_0 = [RhB]_0 = [CBZ]_0 = [BPA]_0 = 10 \text{ mg/L}$; $[TCH]_0 = 20.0 \text{ mg/L}$; $[catalyst]_0 = 0.04 \text{ g/L}$; $[PMS]_0 = 1.0 \text{ mM}$. The light color area around each curve is the corresponding error band.

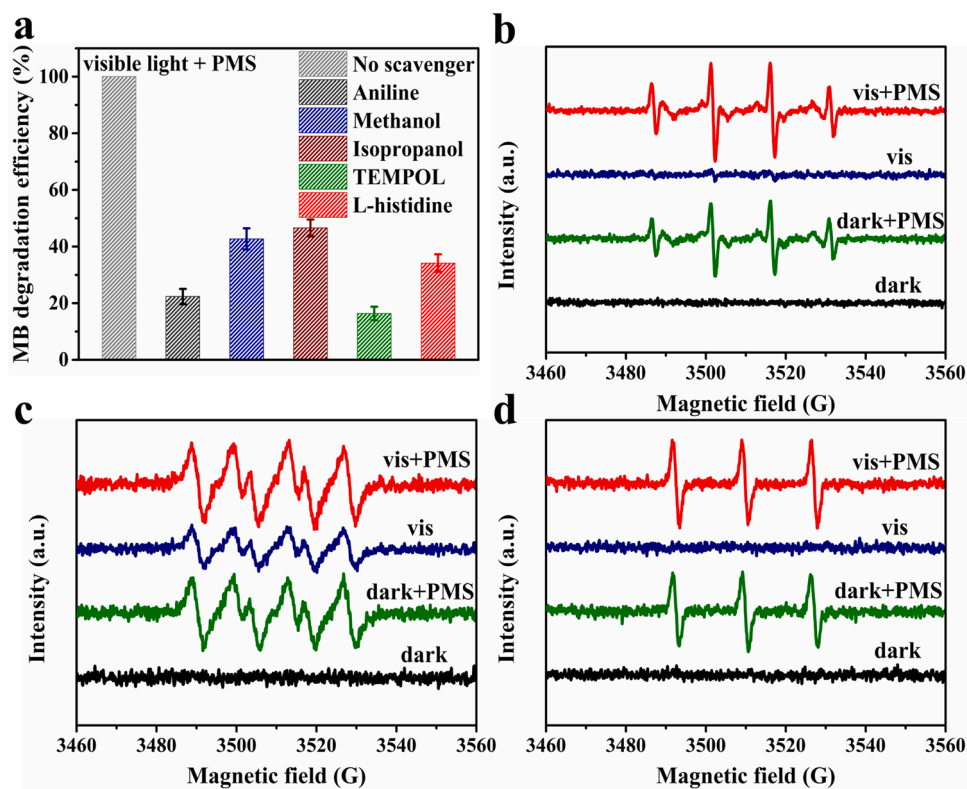


Fig. 3. (a) Reactive species scavenger experiments with CuZnO-3 in the photo-assisted Fenton-like system, and the ESR spectra of CuZnO-3 in different systems (b) $\bullet OH$, $SO_4^{\bullet -}$ -DMPO in water (c) $\bullet O_2^-$ -DMPO in methanol and (d) 1O_2 -TEMP in water.

and first-order MB removal, and the fitting curves were shown in Fig. 2d. The corresponding calculation results (Table S2) showed that the R^2 of all samples is greater than 0.95, indicating a good fitting by pseudo-third-order kinetics.

The CuZnO-3 also had broad-spectrum catalytic degradation ability for typical emerging pollutants (Fig. 2e, and the corresponding curves of C/C_0 with time were given in Fig. S14). The catalytic performance was stronger than that of same-type catalysts recently reported under similar reaction systems with much lower catalyst dosage (Table S3). Recycling tests and Cu leaching assays were performed to determine the reusability and environmental friendliness of CuZnO-3. As shown in Figs. 2f and S15, the catalytic degradation rate of the CuZnO-3 decreased by 13.8% after five cycles. The concentration of the leached Zn and Cu ions of CuZnO-3 was separately 0.70 and 0.24 mg/L in the first cycle, and it declined markedly to 0.28 and 0.06 mg/L after five cycles. This might be ascribed to the releasing of the weakly bounded Cu on CuZnO-3 surface after the chemical oxidation [43]. The leached Cu ion concentration of each cycle test was lower than the emission standard of Zn (2.0 mg/L, GB 8978–1996) and Cu (0.5 mg/L, GB 25467–2010) in China. The phase structure of the catalyst before and after the reaction barely changed, confirmed by the results of XRD and XPS characterization (Fig. S16). The degradation adaptability of CuZnO-3 was also verified in that CuZnO-3 exhibited stable catalytic removal performance in the different reaction environments of wide pH media (5–11), inorganic ions or actual water substrates (Fig. S17 and Text S5). This illustrated the superiority of the co-synthetic preparation method and the construction of bimetallic compound.

3.3. Identification of reactive species

The experimental results of scavenger shown in Fig. 3a with the detailed degradation curves provided in the Fig. S18 confirmed that all the detected reactive species were all responsible for the pollutant degradation, with the contribution in order of $\bullet\text{O}_2^- > \text{SO}_5^{\bullet-} > {}^1\text{O}_2 > \text{SO}_4^{\bullet-} > \bullet\text{OH}$. The ESR test results were in good agreement with the experimental data of reactive species scavenging. The ESR spectra of CuZnO-3 under different conditions were employed to detect the existence of each reactive species in the reaction system. It could be observed from Fig. 3b that the systems with the participation of PMS all exhibited strong $\text{SO}_4^{\bullet-}$ and $\bullet\text{OH}$ signals, which was owing to the rapid activation and decomposition of PMS by the CuZnO-3. In the single photocatalytic system, the $\bullet\text{OH}$ signal was weak. In Fig. 3c, the $\bullet\text{O}_2^-$ characteristic peak with an intensity ratio of 1:1:1:1 was obvious in each system. Fig. 3d illustrated that ${}^1\text{O}_2$ did not exist under visible light irradiation only, but appeared after adding PMS. This suggested that the source of ${}^1\text{O}_2$ was the series of reactions caused by the PMS decomposition. The generation amount of active species in the single Fenton-like system was slightly lower than that in the photo-assisted Fenton-like system, while the pollutant removal capability was far less. This might be due to the fact that the visible light irradiation facilitated the continuous production of active species. Meanwhile, the $\text{SO}_5^{\bullet-}$ which cannot be detected by ESR also played a non-negligible role in the MB decay [44].

3.4. Verification of the S-scheme heterojunction construction

It was generally believed that the charge transfer mode of the S-scheme heterojunction could be verified by the generation of $\bullet\text{O}_2^-$ and $\bullet\text{OH}$ by the catalyst in the photocatalytic reaction system [12]. In the vis/CuZnO-3 system, $\bullet\text{OH}$ and $\bullet\text{O}_2^-$ signals were all observed (Fig. 3b and c), which was consistent with the result of the free radicals scavenging in the photocatalytic system (Fig. S19). Combined with the energy band position data of pristine ZnO calculated from the test results (Figs. S7 and S20) according to the reported method and the previous work on CuO (Table S4), the possible generation mechanism of free radicals was deduced [45,46]. Since the conduction band (CB) energy of pristine ZnO (-0.17 V) was not sufficient to reduce O_2 to $\bullet\text{O}_2^-$

($\text{O}_2/\bullet\text{O}_2^- = -0.33$ V vs. NHE), the $\bullet\text{O}_2^-$ was more likely to be generated in the CB of CuO which possessed a more negative position, while the $\bullet\text{OH}$ ($\text{OH}^-/\bullet\text{OH} = 2.38$ V vs. NHE) could be produced on the higher energy ZnO valence band (VB, 2.97 V). The carriers were retained in the higher-position energy band, rather than transferred to lower ones, which was certain the successful construction of the S-scheme heterojunction. As the related research reported and the test results (Fig. S21 and Text S6) exhibited, the impurity energy level generated by Cu doping could reduce the CB position of ZnO [47]. The electrons on the reduced CB of Cu-doped ZnO were more favorable to combine with holes in the VB of CuO, which was key to the formation of the S-scheme heterojunction.

3.5. PMS activation mechanism by metal sites on CuZnO surface

We performed DFT calculations to elucidate the activation mechanism of different sites on the catalyst surface during PMS activation. The adsorption and decomposition reaction processes of PMS on pristine ZnO and CuZnO composite were separately simulated. The PMS molecule was absorbed and binding on the metal sites of the catalysts. Therefore, in the CuZnO, the Zn sites, Cu sites of CuO phase and dopant Cu sites were denoted as CuZnO*1(ZnO), CuZnO*2(CuO) and CuZnO*3(doped Cu), respectively. The Gibbs free energy profiles and the corresponding intermediate structures at different stages were displayed in Figs. 4 and S22. PMS was first spontaneously adsorbed onto the metal sites in the crystal surface as $^*\text{HOSO}_4$ (II). Then, the O–O bond in the PMS was continuously elongated until broken (III, IV) due to the strong interaction caused by charge accumulation (as shown in the result of charge density difference in Fig. S23) [41,48]. Eventually, free $\text{SO}_4^{\bullet-}$ and $\bullet\text{OH}$ were formed and gradually left the surface of the catalyst (V) [49]. This suggested that in addition to variable-valence metal and photocatalytic activation methods, PMS could also be activated by the adsorption-decomposition which reacted at the strong metallic sites.

Compared to the more electronegative Cu, Zn sites possessed stronger spontaneous adsorption capacity for PMS determined by its highest PMS absorption energy (E_{abs}). This feature was more prominent after the construction of bimetallic oxides, which could be attributed to the fact that additive Cu increased the charge density around the Zn site (Fig. S23). Simultaneously, the energy barrier (ΔE) to overcome for the PMS decomposition was lower on the Cu sites, especially on the CuO phase in CuZnO, indicating that the Cu site was more appropriate for the excitation of PMS. In general, it could be considered that Zn and Cu sites played different roles during the reaction between CuZnO bimetallic oxides with PMS, where the Zn sites were mainly for adsorption, while the Cu sites contributed more to the PMS activation.

The PMS activation pathway independent of photogenerated carriers was not limited to the charge transfer of the binding interaction, and the activation effect of reductive Cu(I) sites in the interface should not be ignored, which was clarified by a scavenger experiment (Fig. S24). After adding DMP (2,9-dimethyl-1,10-phenanthroline) as a Cu(I) scavenger,

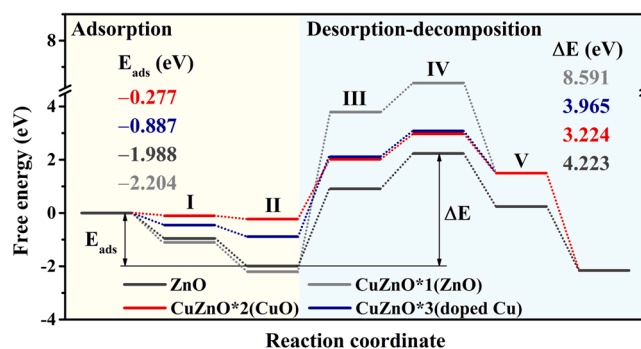


Fig. 4. The Gibbs free energy profiles of PMS adsorption-decomposition mediated by different reactive sites.

the MB removal rate decreased by 62.8%. The relative content of Cu(I) in the CuZnO-3 was decreased by 2.5% after recycling (Fig. S25), confirming the involvement of Cu(I) in the PMS activation, and the less reduced of Cu(I) content might be attributed to the acceleration of the Cu(I)/Cu(II) cycle by the S-scheme heterojunction [9,50]. This certificated that the series of reactions initiated by Cu(I) possessed a significantly effect on the catalytic degradation.

The above results could explain the weak PMS activation ability of CuZnO under dark condition and the necessity of visible light introduction. Under dark condition, the less content Cu sites (~6.7% in the CuZnO-3, provided in Table S5) in the composite catalyst would activate PMS via adsorption-decomposition and electron donation of low-valence Cu(I), contributing most of the PMS activation. However, the Zn sites with higher content (~47.5% in the CuZnO-3) fixed more PMS molecule but could hardly radicalize owing to their high ΔE (8.591 eV). The reduced pollutant degradation rate of the above reaction system (35.9% for MB removal with CuZnO-3, Fig. S8b) could be attributed to the low utilization of active sites. After the introduction of visible light, the enriched hole (h^+) on the ZnO surface would oxidize the PMS strongly bound on the Zn sites to highly active $SO_5^{\cdot-}$, so that the abundant Zn site was fully utilized, promoting the rapid activation of the PMS.

3.6. Proposed reaction mechanism of vis/CuZnO-3/PMS system

The reaction mechanism under the catalyst/vis/PMS system could be described as Fig. 5. The CuZnO-3 obtained by the co-synthesis of Cu and Zn bimetal ions was essentially an S-scheme heterojunction composed of CuO and Cu-doped ZnO, which possessed abundant reactive sites. The metal sites on the catalyst surface could adsorb and radicalize HSO_5^- , among which the Cu sites contributed prominently. The Cu(I) in interface also activated the adsorbed HSO_5^- to generate $SO_4^{\cdot-}$ by electron-donating, while Cu(I) would also reduce O_2 to $\bullet O_2^-$. The photo-generated electrons and holes separately retained on the high-level CB of CuO and VB of Cu-doped ZnO. O_2 and HSO_5^- were reduced on the CB of CuO to produce $\bullet O_2^-$ and $SO_4^{\cdot-}$, respectively. HSO_5^- could also be activated by the generated $\bullet O_2^-$ to form 1O_2 and $SO_4^{\cdot-}$. The $SO_4^{\cdot-}$ radicals would be further transferred into 1O_2 and $\bullet OH$. The enrichment of electrons on CuO could not only facilitate the formation of various free radicals, but also promote the regeneration of Cu(I) and enhance the PMS activation ability of Cu sites. Simultaneously, the holes on the VB of Cu-doped ZnO would take full advantage of the numerous HSO_5^- anchored on the Zn sites. The holes might not only oxidize H_2O to form $\bullet OH$, but also HSO_5^- to produce highly oxidative $SO_5^{\cdot-}$ which could be

converted into $SO_4^{\cdot-}$ and 1O_2 .

Based on the different roles of Cu and Zn sites in bimetallic oxides, the construction of S-scheme heterostructures not only realized the full utilization of high-energy bands, but also demarcated distinct functional regions for oxidation/reduction reactions. This enabled the efficient generation of various reactive species, and effectively suppressed the exciton recombination. The photogenerated carriers were continuously consumed by PMS through oxidation/reduction, promoting the separation of electron-hole pairs, and was beneficial to the synergistic coupling of photocatalysis and PMS activation.

4. Conclusion

In summary, a S-scheme heterojunction constructed by CuO and Cu-doped ZnO was prepared via co-synthesis method, and the energy band of CuO and ZnO possessing strong reduction/oxidation capability was retained. The prepared composite catalyst exhibited excellent catalytic degradation activity in the photo-assisted Fenton-like system. The introduction of Cu is crucial for the improvement of catalytic activation performance due to the following functions: (i) altering the appearance structure of ZnO NPs to supplement surface active sites, (ii) accelerating the generation and transfer of photogenerated charge, and inhibiting the recombination of electron-hole pairs, (iii) providing abundant Cu (I) for electron donating to activate PMS, (iv) enhancing the PMS adsorption capacity of Zn sites and promoting the formation of strong oxidizing $\bullet SO_5^-$. The ZnO acted as a stable substrate for the introduction of Cu and stimulated the reductive activation of PMS at Cu sites. The results of pollutant mineralization and biological toxicity evaluation confirmed that this reaction system could well extend the possibility for the practical application.

CRediT authorship contribution statement

Tianren Li: Data curation, Conceptualization, Investigation, Visualization, Writing – original draft. **Mingyu Li:** Investigation, Validation. **Jingjing Jiang:** Formal analysis. **Ziqing Zhao:** Validation, Writing – review & editing. **Zhongxu Li:** Validation, Writing – review & editing. **Chunrui Zhao:** Funding acquisition, Resources. **Xinyu Wang:** Resources. **Shuangshi Dong:** Funding acquisition, Project administration, Resources, Supervision, Writing – review & editing.

Declaration of Competing Interest

The authors declare that they have no known competing financial

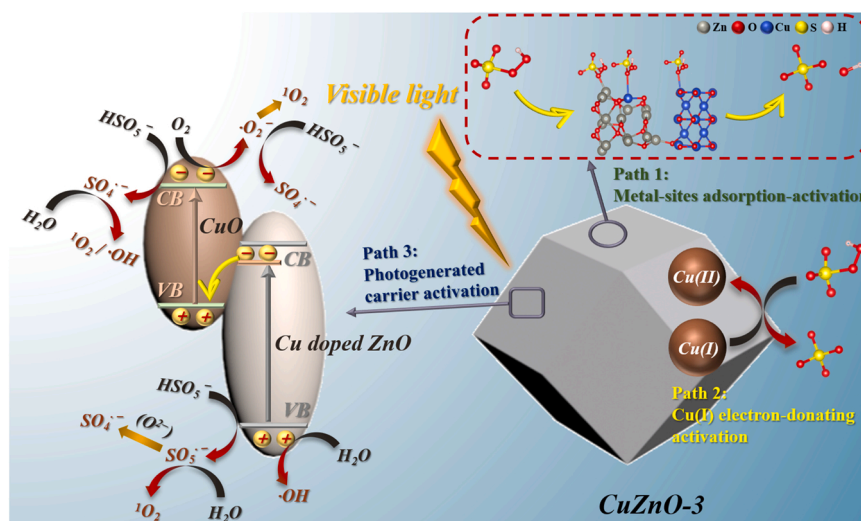


Fig. 5. Possible reaction mechanism with CuZnO-3 in photo-assisted Fenton-like system.

interests or personal relationships that could have appeared to influence the work reported in this paper.

Data availability

Data will be made available on request.

Acknowledgements

This work was financially supported by the National Natural Science Foundation of China (52170079, U20A20322), Science and Technology Development Program of Jilin Province, China (20220508100RC), Natural Science Foundation of Chongqing, China (cstc2021jcyj-msxmX0954, cstc2021jcyj-msxmX1032), and 111 Project (B16020) of Jilin University, China.

Appendix A. Supporting information

Supplementary data associated with this article can be found in the online version at [doi:10.1016/j.apcatb.2023.122539](https://doi.org/10.1016/j.apcatb.2023.122539).

References

- X.Y. Mi, H. Zhong, H.X. Zhang, S.Z. Xu, Y. Li, H.T. Wang, S.H. Zhan, J. C. Crittenden, Facilitating redox cycles of copper species by pollutants in peroxymonosulfate activation, *Environ. Sci. Technol.* 56 (2022) 2637–2646, <https://doi.org/10.1021/acs.est.1c06762>.
- W. Zhao, Z.Y. Duan, Z. Zheng, B. Li, Cobalt bismuth oxide with cobalt(II/III) as a new stable peroxymonosulfate activator for effective degradation, mineralization, and detoxification of diclofenac in water, *J. Clean. Prod.* 365 (2022), 132781, <https://doi.org/10.1016/j.jclepro.2022.132781>.
- F. Chen, G.X. Huang, F.B. Yao, Q. Yang, Y.M. Zheng, Q.B. Zhao, H.Q. Yu, Catalytic degradation of ciprofloxacin by a visible-light-assisted peroxymonosulfate activation system: Performance and mechanism, *Water Res.* 173 (2020), 115559, <https://doi.org/10.1016/j.watres.2020.115559>.
- L. Wang, X. Huang, M. Han, L. Lyu, T. Li, Y.W. Gao, Q.Y. Zeng, C. Hu, Efficient inhibition of photogenerated electron-hole recombination through persulfate activation and dual-pathway degradation of micropollutants over iron molybdate, *Appl. Catal. B: Environ.* 257 (2019), 117904, <https://doi.org/10.1016/j.apcatb.2019.117904>.
- A.A. Isari, S. Moradi, S.S. Rezaei, F. Ghanbari, E. Dehghanifard, B. Kakavandi, Peroxymonosulfate catalyzed by core/shell magnetic ZnO photocatalyst towards malathion degradation: Enhancing synergy, catalytic performance and mechanism, *Sep. Purif. Technol.* 275 (2021), 119163, <https://doi.org/10.1016/j.seppur.2021.119163>.
- H.Q. Sun, S.Z. Liu, S.M. Liu, S.B. Wang, A comparative study of reduced graphene oxide modified TiO₂, ZnO and Ta₂O₅ in visible light photocatalytic/photochemical oxidation of methylene blue, *Appl. Catal. B Environ.* 146 (2014) 162–168, <https://doi.org/10.1016/j.apcatb.2013.03.027>.
- T.R. Li, Y.L. Liu, M.Y. Li, J.J. Jiang, J.Y. Gao, S.S. Dong, Fabrication of oxygen defect-rich pencil-like ZnO nanorods with CDots and Ag co-enhanced photocatalytic activity for tetracycline hydrochloride degradation, *Sep. Purif. Technol.* 266 (2021), 118605, <https://doi.org/10.1016/j.seppur.2021.118605>.
- G.P. Zhang, D.Y. Chen, N.J. Li, Q.F. Xu, H. Li, J.H. He, J.M. Lu, Fabrication of Bi₂MoO₆/ZnO hierarchical heterostructures with enhanced visible-light photocatalytic activity, *Appl. Catal. B Environ.* 250 (2019) 313–324, <https://doi.org/10.1016/j.apcatb.2019.03.055>.
- X.C. Dou, Y.G. Chen, H.F. Shi, CuBi₂O₄/BiOBr composites promoted PMS activation for the degradation of tetracycline: S-scheme mechanism boosted Cu²⁺/Cu⁺ cycle, *Chem. Eng. J.* 431 (2022), 134054, <https://doi.org/10.1016/j.cej.2021.134054>.
- S. Chen, Y.Y. Rong, L.L. Tu, Z.B. Yu, H.X. Zhu, S.F. Wang, Y.P. Hou, Coupling the bioanode and S-scheme CuO/CdS quantum dots photocathode for chlortetracycline degradation: Performance, mechanism and microbial community, *Process Saf. Environ. Prot.* 166 (2022) 328–340, <https://doi.org/10.1016/j.psep.2022.08.037>.
- S.X. Wang, J.Y. Tian, Q. Wang, F. Xiao, S.S. Gao, W.X. Shi, F.Y. Cui, Development of CuO coated ceramic hollow fiber membrane for peroxymonosulfate activation: a highly efficient singlet oxygen-dominated oxidation process for bisphenol A degradation, *Appl. Catal. B Environ.* 256 (2019), 117783, <https://doi.org/10.1016/j.apcatb.2019.117783>.
- Q.L. Xu, L.Y. Zhang, B. Cheng, J.J. Fan, J.G. Yu, S-scheme heterojunction photocatalyst, *Chem* 6 (2020) 1543–1559, <https://doi.org/10.1016/j.chempr.2020.06.010>.
- P. Bharathi, S. Harish, J. Archana, M. Navaneethan, S. Ponnusamy, C. Muthamizhchelvan, M. Shimomura, Y. Hayakawa, Enhanced charge transfer and separation of hierarchical CuO/ZnO composites: The synergistic effect of photocatalysis for the mineralization of organic pollutant in water, *Appl. Surf. Sci.* 484 (2019) 884–891, <https://doi.org/10.1016/j.apsusc.2019.03.131>.
- V. Vaianoa, G. Iervolino, L. Rizzo, Cu-doped ZnO as efficient photocatalyst for the oxidation of arsenite to arsenate under visible light, *Appl. Catal. B Environ.* 238 (2018) 471–479, <https://doi.org/10.1016/j.apcatb.2018.07.026>.
- F.A. Qaraah, S.A. Mahyoub, A. Hezam, A. Qaraah, Q.A. Drmash, G.L. Xiu, Construction of 3D flowers-like O-doped g-C₃N₄/N-doped Nb₂O₅/C heterostructure with direct S-scheme charge transport and highly improved visible-light-driven photocatalytic efficiency, *Chin. J. Catal.* 43 (2022) 2637–2651, [https://doi.org/10.1016/S1872-2067\(21\)64038-X](https://doi.org/10.1016/S1872-2067(21)64038-X).
- A.N. Kadam, T.G. Kim, D.S. Shin, K.M. Garadkar, J. Park, Morphological evolution of Cu doped ZnO for enhancement of photocatalytic activity, *J. Alloy. Compd.* 710 (2017) 102–113, <https://doi.org/10.1016/j.jallcom.2017.03.150>.
- S. Payra, S. Challagulla, Y. Bobde, C. Chakraborty, B. Ghosh, S. Roy, Probing the photo- and electro-catalytic degradation mechanism of methylene blue dye over ZIF-derived ZnO, *J. Hazard. Mater.* 373 (2019) 377–388, <https://doi.org/10.1016/j.jhazmat.2019.03.053>.
- J.Y. Chen, A.T. Gu, E.D. Miensah, Y. Liu, P. Wang, P. Mao, C.H. Gong, Y. Jiao, K. Chen, Y. Yang, Cu-Zn bimetal ZIFs derived nanowhisker zero-valent copper decorated ZnO nanocomposites induced oxygen activation for high-efficiency iodide elimination, *J. Hazard. Mater.* 416 (2021), 126097, <https://doi.org/10.1016/j.jhazmat.2021.126097>.
- H. Dai, X.Z. Yuan, L.B. Jiang, H. Wang, J. Zhang, J.J. Zhang, T. Xiong, Recent advances on ZIF-8 composites for adsorption and photocatalytic wastewater pollutant removal: Fabrication, applications and perspective, *Coord. Chem. Rev.* 441 (2021), 213985, <https://doi.org/10.1016/j.ccr.2021.213985>.
- B.Y. Qi, X.C. Wang, X.Y. Wang, J.P. Cheng, Y.Y. Shang, Synthesis and H₂S-Sensing Properties of MOF-Derived Cu-Doped ZnO Nanocages, *Nanomater.* -basel 12 (2022) 2579, <https://doi.org/10.3390/nano12152579>.
- G. Ko, S. Park, W. Kim, K. Kwon, Synergistic effect of Na and Al co-doping on the electrochemical properties of Li[Ni_{0.8}Mn_{0.1}Co_{0.1}]O₂ cathode materials for Li-ion batteries, *J. Alloy. Compd.* 925 (2022), 166678, <https://doi.org/10.1016/j.jallcom.2022.166678>.
- N.T. Hanh, N.L.M. Tri, D. Van Thuan, M.H.T. Tung, T.-D. Pham, T.D. Minh, H. T. Trang, M.T. Binh, M.V. Nguyen, Monocrotophos pesticide effectively removed by novel visible light driven Cu doped ZnO photocatalyst, *J. Photochem. Photobiol. A* 382 (2019), 111923, <https://doi.org/10.1016/j.jphotochem.2019.111923>.
- Z.W. Ge, C.L. Wang, T. Chen, Z.Y. Chen, T. Wang, L. Guo, G.G. Qi, J.Q. Liu, Preparation of Cu-doped ZnO nanoparticles via layered double hydroxide and application for dye-sensitized solar cells, *J. Phys. Chem. Solids* 150 (2021), 109833, <https://doi.org/10.1016/j.jpcs.2020.109833>.
- E. Abbasi, M. Haghighi, R. Shokrani, M. Shabani, Copper plasmon-induced Cu-doped ZnO-CuO double-nanoheterojunction: In-situ combustion synthesis and photo-decontamination of textile effluents, *Mater. Res. Bull.* 129 (2020), 110880, <https://doi.org/10.1016/j.materresbull.2020.110880>.
- R.K. Chava, M. Kang, Improving the photovoltaic conversion efficiency of ZnO based dye sensitized solar cells by indium doping, *J. Alloy. Compd.* 692 (2017) 67–76, <https://doi.org/10.1016/j.jallcom.2016.09.029>.
- S.S. Mohtar, F. Aziz, A.F. Ismail, N.S. Sambudi, H. Abdullah, A.N. Rosli, B. Ohtani, Impact of doping and additive applications on photocatalyst textural properties in removing organic pollutants: a review, *Catalysts* 11 (2021) 1160, <https://doi.org/10.3390/catal11101160>.
- L.L. Zhao, J.M. Zhang, Z.P. Zhang, J. Feng, T. Wei, Y.M. Ren, Y.J. Zhu, J. Ma, CuO with (001)-plane exposure efficiently induces peroxymonosulfate to form =Cu-OOSO₂ intermediates directly oxidizing organic contaminants in water, *Chem. Eng. J.* 441 (2022), 136100, <https://doi.org/10.1016/j.cej.2022.136100>.
- G. Gao, Y. Su, X. Quan, V.K. Sharma, S. Chen, H.T. Yu, Y.B. Zhang, J.F. Niu, Electronic modulation of iron-bearing heterogeneous catalysts to accelerate Fe(III)/Fe(II) redox cycle for highly efficient Fenton-like catalysis, *Appl. Catal. B Environ.* 276 (2020), 119016, <https://doi.org/10.1016/j.apcatb.2020.119016>.
- P.P. Huang, L.L. Yao, Q. Chang, Y.H. Sha, G.D. Jiang, S.H. Zhang, Z. Li, Room-temperature preparation of highly efficient NH₂-MIL-101(Fe) catalyst: The important role of -NH₂ in accelerating Fe(III)/Fe(II) cycling, *Chemosphere* 291 (2022), 133026, <https://doi.org/10.1016/j.chemosphere.2021.133026>.
- D. Tolomana, A. Popaa, M. Stana, M. Stefana, G. Vladb, S. Ulinicib, G. Baisanb, T. D. Silipasa, S. Macaveia, C. Leosteanu, S. Pruneanu, F. Pogaceanu, R.C. Suciu, L. Barbu-Tudorana, O. Pana, Visible-light-driven photocatalytic degradation of different organic pollutants using Cu doped ZnO-MWCNT nanocomposites, *J. Alloy. Compd.* 866 (2021), 159010, <https://doi.org/10.1016/j.jallcom.2021.159010>.
- S. Ghosh, R. Das, S. Kundu, M.K. Naskar, Emulsion based solvothermal synthesis of CuO grainy rod via the formation of quasi-quadrangular prism shaped Cu₂(OH)₃Br for recyclable catalyst of 4-nitrophenol reduction, *J. Phys. Chem. Solids* 147 (2020), 109551, <https://doi.org/10.1016/j.jpcs.2020.109551>.
- Y.T. Liu, Q.P. Zhang, M. Xu, H. Yuan, Y. Chen, J.X. Zhang, K.Y. Luo, J.Q. Zhang, B. You, Novel and efficient synthesis of Ag-ZnO nanoparticles for the sunlight-induced photocatalytic degradation, *Appl. Surf. Sci.* 476 (2019) 632–640, <https://doi.org/10.1016/j.apsusc.2019.01.137>.
- S. Shao, X.S. Li, Z.M. Gong, B. Fan, J.H. Hu, J.B. Peng, K. Lu, S.X. Gao, A new insight into the mechanism in Fe₃O₄@CuO/PMS system with low oxidant dosage, *Chem. Eng. J.* 438 (2022), 135474, <https://doi.org/10.1016/j.cej.2022.135474>.
- Z.X. Pei, L.Y. Ding, J. Hu, S.X. Weng, Z.Y. Zheng, M.L. Huang, P. Liu, Defect and its dominance in ZnO films: a new insight into the role of defect over photocatalytic activity, *Appl. Catal. B: Environ.* 142–143 (2013) 736–743, <https://doi.org/10.1016/j.apcatb.2013.05.055>.
- S. Bai, N. Zhang, C. Gao, Y.J. Xiong, Defect engineering in photocatalytic materials, *Nano Energy* 53 (2018) 296–336, <https://doi.org/10.1016/j.nanoen.2018.08.058>.

- [36] M. Nolan, A. Iwaszuk, A.K. Lucid, J.J. Carey, M. Fronzi, Design of Novel Visible Light Active Photocatalyst Materials: Surface Modified TiO₂, *Adv. Mater.* 28 (2016) 5425–5446, <https://doi.org/10.1002/adma.201504894>.
- [37] J.J. Jiang, X.Y. Wang, Y. Liu, Y.H. Ma, T.R. Li, Y.H. Lin, T.F. Xie, S.S. Dong, Photo-Fenton degradation of emerging pollutants over Fe-POM nanoparticle/porous and ultrathin g-C₃N₄ nanosheet with rich nitrogen defect: Degradation mechanism, pathways, and products toxicity assessment, *Appl. Catal. B: Environ.* 278 (2020), 119349, <https://doi.org/10.1016/j.apcatb.2020.119349>.
- [38] M.I. Maldonado, E. Saggioro, J. Peral, E. Rodríguez-Castellón, J. Jiménez-Jiménez, S. Malato, Hydrogen generation by irradiation of commercial CuO + TiO₂ mixtures at solar pilot plant scale and in presence of organic electron donors, *Appl. Catal. B: Environ.* 257 (2019), 117890, <https://doi.org/10.1016/j.apcatb.2019.117890>.
- [39] A. Molla, M. Sahu, S. Hussain, Under dark and visible light: fast degradation of methylene blue in the presence of Ag–In–Ni–S nanocomposites, *J. Mater. Chem. A* 3 (2015) 15616–15625, <https://doi.org/10.1039/C5TA02888D>.
- [40] C.X. Fu, M. Yan, Z.Y. Wang, J. Li, X.L. Zhang, W. Song, Z.L. Xu, K. Bhatt, Z. M. Wang, S.N. Zhu, New insights into the degradation and detoxification of methylene blue using heterogeneous-Fenton catalyzed by sustainable siderite, *Environ. Res.* 216 (2023), 114819, <https://doi.org/10.1016/j.envres.2022.114819>.
- [41] J.J. Jiang, Z.Q. Zhao, J.Y. Gao, T.R. Li, M.Y. Li, D.D. Zhou, S.S. Dong, Nitrogen vacancy-modulated peroxymonosulfate nonradical activation for organic contaminant removal via high-valent cobalt-oxo species, *Environ. Sci. Technol.* 56 (2022) 5611–5619, <https://doi.org/10.1021/acs.est.2c01913>.
- [42] Z.Y. Choong, M.F. Gasim, K.Y.A. Lin, T.S. Hamidon, H. Hussin, W.D. Oh, Unravelling the formation mechanism and performance of nitrogen, sulfur codoped biochar as peroxymonosulfate activator for gatifloxacin removal, *Chem. Eng. J.* 451 (2023), 138958, <https://doi.org/10.1016/j.cej.2022.138958>.
- [43] J.J. Jiang, X.Y. Wang, C.J. Zhang, T.R. Li, Y.H. Lin, T.F. Xie, S.S. Dong, Porous OD/3D NiCo₂O₄/g-C₃N₄ accelerate emerging pollutant degradation in PMS/vis system: Degradation mechanism, pathway and toxicity assessment, *Chem. Eng. J.* 397 (2020), 125356, <https://doi.org/10.1016/j.cej.2020.125356>.
- [44] L.Z. Huang, X.L. Wei, E.L. Gao, C.B. Zhang, X.M. Hu, Y.Q. Chen, Z.Z. Liu, N. Finck, J. Lützenkirchen, D.D. Dionysiou, Single Fe atoms confined in two-dimensional MoS₂ for sulfite activation: A biomimetic approach towards efficient radical generation, *Appl. Catal. B: Environ.* 268 (2020), 118459, <https://doi.org/10.1016/j.apcatb.2019.118459>.
- [45] C.K. Yao, R. Wang, Z.S. Wang, H. Lei, X.P. Dong, C.Z. He, Highly dispersive and stable Fe³⁺ active sites on 2D graphitic carbon nitride nanosheets for efficient visible-light photocatalytic nitrogen fixation, *J. Mater. Chem. A* 7 (2019) 27547–27559, <https://doi.org/10.1039/C9TA09201C>.
- [46] C.L. Yue, J.J. Jiang, M.Y. Li, X.Y. Wang, T.R. Li, Z.Q. Zhao, S.S. Dong, Accelerating the peroxymonosulfate activation and charge transfer by construction of Fermi energy level-matched CoWO₄/g-C₃N₄ photocatalyst for typical antibiotics degradation, *Sep. Purif. Technol.* 301 (2022), 122020, <https://doi.org/10.1016/j.seppur.2022.122020>.
- [47] K.V. Karthik, A.V. Raghu, K.R. Reddy, R. Ravishankar, M. Sangeeta, N.P. Shetti, C. V. Reddy, Green synthesis of Cu-doped ZnO nanoparticles and its application for the photocatalytic degradation of hazardous organic pollutants, *Chemosphere* 287 (2022), 132081, <https://doi.org/10.1016/j.chemosphere.2021.132081>.
- [48] Q. Gao, H.T. Li, X.Z. Wang, B. Han, K.S. Xia, J.P. Wu, C.G. Zhou, J. Dong, Doping phosphorus into Co₃O₄: A new promising pathway to boost the catalytic activity for peroxymonosulfate activation, *Appl. Surf. Sci.* 574 (2022), 151632, <https://doi.org/10.1016/j.apsusc.2021.151632>.
- [49] H. Liang, R.P. Liu, C.Z. Hu, X.Q. An, X.W. Zhang, H.J. Liu, J.H. Qu, Synergistic effect of dual sites on bimetal-organic frameworks for highly efficient peroxide activation, *J. Hazard. Mater.* 406 (2021), 124692, <https://doi.org/10.1016/j.jhazmat.2020.124692>.
- [50] L.Q. Xua, L.H. Zhao, Y.F. Mao, Z. Zhou, D.L. Wu, Enhancing the degradation of bisphenol A by dioxygen activation using bimetallic Cu/Fe@zeolite: Critical role of Cu(I) and superoxide radical, *Sep. Purif. Technol.* 253 (2020), 117550, <https://doi.org/10.1016/j.seppur.2020.117550>.